Mechanics of pressure-adaptive honeycomb and its application to wing morphing

2011 Smart Mater. Struct. 20 094010

(http://iopscience.iop.org/0964-1726/20/9/094010)

Smart Mater. Struct. **20** (2011) 094010 (11pp) doi:10.1088/0964-1726/20/9/094010

Mechanics of pressure-adaptive honeycomb and its application to wing morphing*

Roelof Vos[1] **and Ron Barrett**[2]

[1] Faculty of Aerospace Engineering, TU Delft, The Netherlands
[2] Department of Aerospace Engineering, The University of Kansas, USA

E-mail: r.vos@tudelft.nl

Received 4 March 2011, in final form 6 July 2011
Published 30 August 2011
Online at stacks.iop.org/SMS/20/094010

Abstract
Current, highly active classes of adaptive materials have been considered for use in many different aerospace applications. From adaptive flight control surfaces to wing surfaces, shape-memory alloy (SMA), piezoelectric and electrorheological fluids are making their way into wings, stabilizers and rotor blades. Despite the benefits which can be seen in many classes of aircraft, some profound challenges are ever present, including low power and energy density, high power consumption, high development and installation costs and outright programmatic blockages due to a lack of a materials certification database on FAR 23/25 and 27/29 certified aircraft. Three years ago, a class of adaptive structure was developed to skirt these daunting challenges. This pressure-adaptive honeycomb (PAH) is capable of extremely high performance and is FAA/EASA certifiable because it employs well characterized materials arranged in ways that lend a high level of adaptivity to the structure. This study is centered on laying out the mechanics, analytical models and experimental test data describing this new form of adaptive material. A directionally biased PAH system using an external (spring) force acting on the PAH bending structure was examined. The paper discusses the mechanics of pressure adaptive honeycomb and describes a simple reduced order model that can be used to simplify the geometric model in a finite element environment. The model assumes that a variable stiffness honeycomb results in an overall deformation of the honeycomb. Strains in excess of 50% can be generated through this mechanism without encountering local material (yield) limits. It was also shown that the energy density of pressure-adaptive honeycomb is akin to that of shape-memory alloy, while exhibiting strains that are an order of magnitude greater with an energy efficiency close to 100%. Excellent correlation between theory and experiment is demonstrated in a number of tests. A proof-of-concept wing section test was conducted on a 12% thick wing section representative of a modern commercial aircraft winglet or flight control surface with a 35% PAH trailing edge. It was shown that camber variations in excess of 5% can be generated by a pressure differential of 40 kPa. Results of subsequent wind tunnel test show an increase in lift coefficient of 0.3 at 23 m s^{-1} through an angle of attack from $-6°$ to $+20°$.

(Some figures in this article are in colour only in the electronic version)

Nomenclature

c	Chord	m
c_d	Section drag coefficient	—
c_l	Section lift coefficient	—
c_m	Section moment coefficient	—
c_p	Pressure coefficient	—
C_L	Wing or vehicle lift coefficient	—
D	Drag	N
E	Young's modulus	N m^{-2}
$\bar{E}$	Equivalent Young's modulus	N m^{-2}
F	Force	N
l	Honeycomb face length	m

* This paper was originally presented at the 2010 ASME SMASIS conference, as paper 'SMASIS 2010-3634'. Despite the substantial changes that have been made to the paper, there are still various figures and text stemming from the original.

L	Lift	N
m	Mass	kg
M	Moment or Mach number	N m, —
p	Pressure	N m^{-2}
R	Gas constant for air	J kg^{-1} K^{-1}
Re	Reynolds number	—
s	Displacement	m
S	Surface area	m^2
t	Thickness	m
T	Temperature	°C
V	Velocity or volume	m s^{-1}, m^3
W	Work	J
Greek symbols		
α	Angle of attack	deg
ε	Strain	—
ζ	Pouch-to-honeycomb volume ratio	—
θ	Honeycomb angle	deg
σ	Normal stress	Pa
φ	Force angle	deg
Subscripts and superscripts		
eq	Equivalent	
ex	External	
i	Initial	
m	Constant mass	
p	Constant pressure	
x, y, z	Principal axis directions	
∞	Free stream	
Abbreviations		
CS	Certification specification	
CDP	Cell differential pressure	
CMT	Cellular material theory	
EASA	European Aviation Safety Authority	
FAA	Federal Aviation Authority	
FAR	Federal Aviation Regulation	
PAH	Pressure adaptive honeycomb	
TO	Takeoff	

1. Introduction

The aircraft design process is typically a compromise between widely disparate flight states. During takeoff and landing, wings should possess high maximum lift coefficients, in cruise lift-to-drag (L/D) ratio dominates. There are many ways to achieve high C_{Lmax} values, but, in general, they involve shapes and mechanisms to keep the wing flow attached at ever higher angles of attack. Often these involve high lift devices, gross changes in wing area, jet slots and changes in wing sweep. To maintain high L/D values, all high lift and chord-extension devices are generally retracted, the aircraft typically flies at altitudes and airspeeds which lead to fairly high C_{L} values, which in turn result in good L/D, which is critical for maintenance of low fuel burn rates. Although traditional high lift devices clearly work, they are often quite complex, comparatively heavy, expensive to fabricate and inspection and maintenance intensive.

More recent developments in high-subsonic aircraft show a shift from complicated high lift devices to simpler structures that consist of fewer parts and have fewer hinging and sliding components. For its A350 Airbus selected a relatively simple single-slotted dropped-hinge flap system [1]. For the 747–8 Boeing decided to replace the triple-slotted Fowler flap system, like those on earlier 747 models, of the inboard wing with a double-slotted system, while the outboard section only utilized a single-slotted system. Both examples illustrate the drive for simpler structures that lead to reduced part count, manufacturing cost and maintenance. In addition, reducing the number of slots between the individual components also reduces the jet-slot noise, which reduces the noise signature of the aircraft, which is critical during landing to meet FAR/CS noise regulations and aid with community acceptance.

Kinematically simple high lift devices place some daunting constraints on aerodynamicists and structural engineers. Because maintaining a small wing area (and resulting high wing loading) is critical for maintenance of high L/D in cruise, mechanisms which induce chord (or span) growth must be capable of fully retracting. Without the design freedom of multiple slots, great pains must be taken to ensure that high C_{LmaxL} and C_{LmaxTO} are not adversely affected. Given that chord (and span) growth typically leads to high levels of mechanical complexity, and slots generate unwanted acoustic signatures, the simplest means of high C_{Lmax} generation is through camber manipulation. Although the lay-engineer may see changes in camber as being equivalent to plain flap deflection, nothing could be farther from the truth from an aerodynamics perspective. Conventional plain flaps generate a suction peak (with associated adverse pressure gradient) at their leading edges during deployment. It is at this location that an already thick boundary layer typically separates, which, in turn, destroys the desired increment in C_{Lmax}. To skirt this problem, a new class of adaptive structures has been invented which can make skins change their curvature in a gradual manner, which in turn reduces the highly adverse pressure gradient (experienced with conventional flaps), and allows the airfoil to possess C_{Lmax} values which are much higher than a plain airfoil could ever experience. There are many examples in the literature that detail mechanisms that induce these camber variations. Successful demonstrations of this technology include the mission adaptive wing [2] and the DARPA smart wing program [3]. Under the European SADE project various morphing mechanisms and skins are being investigated [4].

Although it is possible to induce gross changes in camber in a stand-alone airfoil section, it is also possible to effect changes in sections of flaps themselves. Although the concept has been debated for some time, typically highly cambered flaps are not found because there are neither conventional mechanical devices which can actuate such an aerodynamic section, nor adaptive materials which can generate strain levels of the order of 50%, which is required to make such a concept feasible. Such flaps can indeed induce nontrivial increases in C_{Lmax}, and would function as seen in figure 1.

Further, nearly all classes of adaptive materials currently lack an FAA recognized certification database (like Mil-Hdbk-5) which would allow them to be used in FAR 23/25 (normal, commuter, aerobatic, agricultural, and large airplanes) and FAR 27/29 (small and large helicopters) certified aircraft.

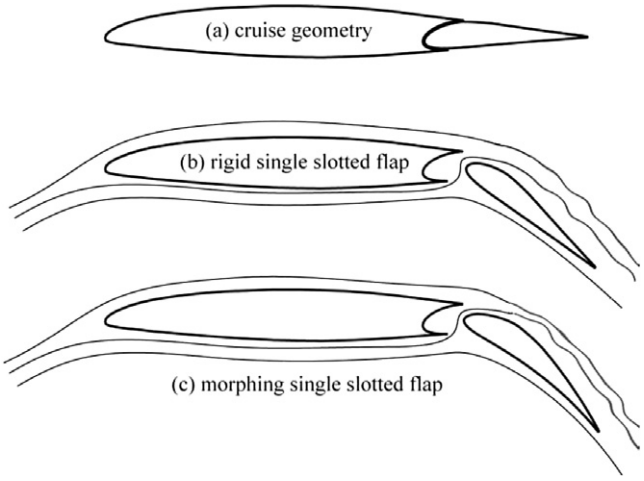

Figure 1. Flap camber increase through gross deformations for induction of flow attachment at higher turning angles.

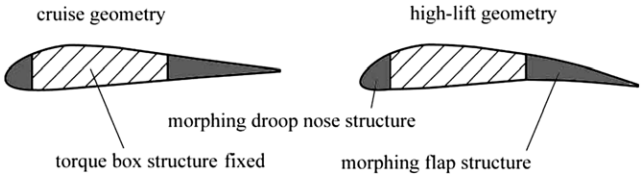

Figure 2. Cruise and low-speed PAH wing, flap or winglet cross-sections.

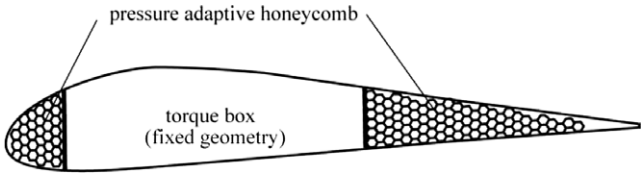

Figure 3. Sketch of the PAH general arrangement with active nose and flap sections.

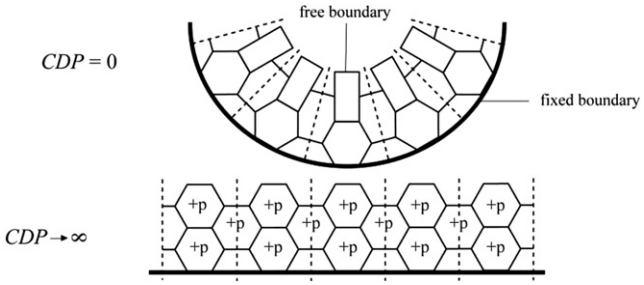

Figure 4. Conceptual working principles behind PAH working an active skin curving mechanism.

Accordingly, the paper will lay out a new hybrid composite material which is certifiable, generates extremely large strains, is comparable to conventional aerospace materials in density, stiffness and strength, consumes very little power, possesses self-diagnosis and repair capability and is comparable in price to conventional aerospace structures.

2. Application of pressure-adaptive honeycomb

Although there are many different families and classes of adaptive materials, few can generate the active strain levels required for gross structural deformations. Even fewer are FAA/EASA certifiable. Because pressure-adaptive honeycomb (PAH) was specifically developed for FAR 23/25 and 27/29 certified aircraft, it possesses all of the most desirable characteristics of conventional aerospace materials along with activity levels which are orders of magnitude larger than conventional adaptive materials. Although various implementations of pressure-adaptive structures are available in the literature (e.g. [5] and [6]), this paper introduces a new incarnation of this technique in a representative structure and demonstrates how it could potentially be used in a morphing flap design to accomplish high lift coefficients on high-subsonic aircraft while complying with the constraints on part count, complexity, and the ability to be certified according to FAR/CS 25 standards. To ensure that the torque box of the flap maintains its structural stiffness and rigidity the following model problem is chosen. A flap or winglet with a morphing trailing edge over the aft 35% of the airfoil is considered together with a morphing drooped leading edge such as shown in figure 2. This requires the pressure-adaptive honeycomb to fit within these designated form factors and spaces.

In figure 3 a schematic representation of the honeycomb arrangement within the flap structure is shown. The PAH acts as a distributed adaptive actuator that does not require hard points to transfer the pressure loads toward the main torque box structure or ribs. By attaching the honeycomb to either one of the skins (top or bottom) it is allowed to freely contract or expand on the opposite side (as shown in figure 4). In this case the initial shape is already curved. This can, for instance, be realized by utilizing a curved skin. The honeycomb is then partially compressed. When a cell differential pressure (CDP) is applied, the pressure inside the cells changes the shape of the honeycomb to a cell shape which is as close as possible to a perfect circle. In this case, the shape is a perfect hexagon (as seen in honeycomb). In the case of the flap or winglet section, this requires the skin on the non-fixed side of the adaptive trailing edge in order to expand and contract in correspondence to the curvature change. Such morphing skins have been successfully designed and applied to a number of morphing aerospace structures [7].

3. Pressure adaptive honeycomb (PAH) mechanics

Pressure adaptive honeycomb utilizes plain honeycomb with cells that extend or contract a significant length in various directions when activated. In each of the cells resides a bladder which can be pressurized such that it changes the overall stiffness and shape of the honeycomb. When an external force is acting on the honeycomb it results in a particular amount of deformation. By altering the cell pressure (and therefore the stiffness) the PAH deformation can be accurately controlled. The honeycomb geometry allows the designer to

accurately predict the amount of deformation based on a given loading case and boundary conditions. By changing the cell size (in terms of wall thickness and wall length) the designer can vary the ratio between the stiffness of the honeycomb in unpressurized and in pressurized conditions. These parameters allow for optimal tailoring of the PAH, which is currently being investigated.

In a finite element environment it is typically desired to map the stiffness properties that are introduced through the pressurization onto the actual honeycomb connecting elements. This allows the designer to evaluate the structural properties of a pressure-adaptive structure (and the material within) without actually having to define the problem in terms of separate air bladders with pressure loadings on them. Instead the properties of the honeycomb structure can be determined and the original material stiffness can be replaced by a new equivalent stiffness (E^{eq}) which is the sum of the original material stiffness (E^{m}) and the pressure-induced stiffness (E^{p}). The following sections show development of the equivalent stiffnesses. The basic model is then used to predict the behavior of several structures against which experimental data are compared.

3.1. Analytic model of rigid-wall PAH

3.1.1. Model structure and assumptions. In order to separate the interaction between the honeycomb and the pouches within (which could lead to Coulomb friction effects) an energy approach is taken that relates the change in pressurized volume to the mechanical work. Because the total volume is of importance, rather than the deformation of the individual ligaments (or cell walls), the following geometric simplification is proposed. Each cell is represented by a hexagon of rigid walls that are connected to each other by means of frictionless hinges in the corners. The reader can verify that such a structure by itself (not pressurized) does not have any stiffness. Any resistance to deformation therefore stems from the addition of the pressurized volumes inside the honeycomb. For a small thickness-to-length ratio (i.e. $t/l \ll 1$) this approximation yields kinematic relations that are very close to those of actual thin-walled honeycomb.

The ratio between pouch volume and hexagon volume is denoted by ζ and is set to the ratio of a circle inside a perfect hexagon (i.e. $\theta_{\mathrm{i}} = 60°$): $\zeta = \sqrt{\pi}/6 \approx 0.91$. It has been experimentally demonstrated that this value is in reality a minimum and that upon deformation the pouch-to-cell volume ratio increases [8]. For the stiffness relation that is derived in the subsequent sections this ratio will appear as a factor that multiplies with the pressure. The choice to fix this parameter has been made to simplify the subsequent analysis. By fixing ζ at its minimum value a conservative assumption is made about the pressure-induced stiffness.

3.1.2. Force–displacement relation for constrained pressurized volumes. A pressure differential over the cell walls of the honeycomb induces an increased stiffness in the total structure. In an attempt to quantify this increased stiffness, the assumption is made that the volumetric change of ordinary honeycomb as a result of a particular deformation is very close to the volumetric change of a honeycomb structure that consists of rigid members connected by frictionless hinges. Based on that assumption a relatively simple model is created that relates the deformation, through the wall angle, θ, to the volumetric change of the honeycomb. This volumetric change, in turn, is opposed by the pressure differential which exists over the cell walls. This opposing force is felt as an increase in overall stiffness due to pressure, $\bar{E}^{\mathrm{p}}$.

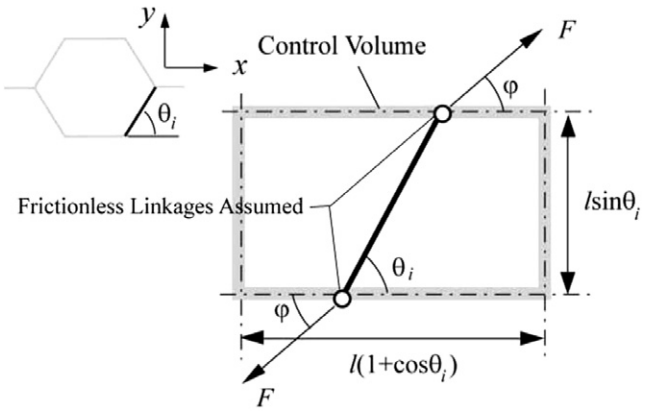

Figure 5. Forces on an incremental section stemming from normal stresses.

If a honeycomb structure of rigid members and frictionless hinges is considered, then the smallest incremental unit that repeats itself within the structure is a z-section with dimensions $l(1+\cos\theta_{\mathrm{i}})$ and $l\sin\theta_{\mathrm{i}}$, where θ_{i} is the initial honeycomb angle. The volume of this unit z-section is calculated according to (see figure 5)

$$V = \zeta l^2 \sin\theta(1+\cos\theta). \tag{1}$$

When an external stress field is applied to the overall structure, the discrete forces on the diagonal members of this z-section can be deduced. This is schematically shown in figure 5. The combination of a stress component in the x-direction and a stress component in the y-direction leads to a discrete force, F, on the diagonal member. The magnitude of this force and its direction (φ) can be related to the overall stress according to the following relations:

$$\sigma_x = \frac{F\cos\varphi}{l\sin\theta_{\mathrm{i}}}, \tag{2}$$

$$\sigma_y = \frac{F\sin\varphi}{l(1+\cos\theta_{\mathrm{i}})}. \tag{3}$$

Knowing that the control volume, V, of figure 5 is pressurized, the work that needs to be done in order to alter the volume (denoted as 'useful' work in [9]) can be expressed as

$$W_{\mathrm{use}} = \int_{V_{\mathrm{i}}}^{V} p\,\mathrm{d}V - p_{\mathrm{a}}(V - V_{\mathrm{i}}), \tag{4}$$

where V_{i} is the initial volume. When the pressure in the cells is kept constant this integral can be evaluated as follows:

$$W_{\mathrm{use}} = (p - p_{\mathrm{a}})(V - V_{\mathrm{i}}). \tag{5}$$

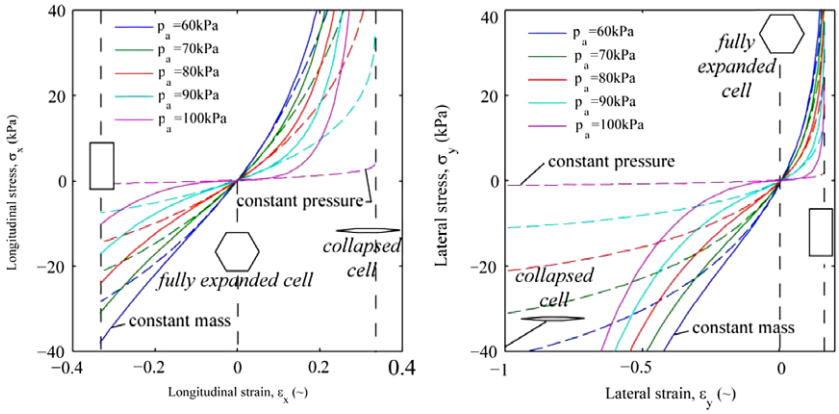

Figure 6. Stress variation with strain at various ambient pressures ($p = 100$ kPa).

When the mass inside the pouches is kept constant, the integral in equation (4) is evaluated as follows:

$$W_{\text{use}} = mRT \ln\left(\frac{V}{V_{\text{i}}}\right) - p_{\text{a}}(V - V_{\text{i}}). \tag{6}$$

These two cases correspond with two individual types of actuation and corresponding system architectures. In the first case (corresponding to the useful work in equation (5)) the pressure is actively controlled. This can be done through a tubing system which connects through a system of valves to one of the compressor stages of the engine. The latter case (corresponding to the useful work in equation (6)) requires less system architecture and relies on a natural pressure difference between the fixed amount of air within the pouch and the ambient pressure. When a typical jet transport ascends to cruise altitude, the ambient pressure decreases and the cell differential pressure increases. This allows the morphing structure to appropriately adapt to a change in altitude without the interference of the pilot.

This useful work should be balanced by the work done by the external force F over a particular distance, s, aligned with the direction of F:

$$W_{\text{ex}} = \int_s F \, \mathrm{d}s. \tag{7}$$

Appropriate substitution in equation (7) and integration between θ_{i} and θ results in the following expression for the external work:

$$W_{\text{ex}} = Fl[\cos(\theta - \varphi) - \cos(\theta_{\text{i}} - \varphi)]. \tag{8}$$

From the balance between the external work (equation (8)) and the useful work (equations (5) and (6), respectively) the relation between the external force, the direction of the force, and the cell differential pressure can be divined:

$$F_{\text{pressure=const}} = \frac{1}{l} \frac{(p - p_{\text{a}})(V - V_{\text{i}})}{\cos(\theta - \varphi) - \cos(\theta_{\text{i}} - \varphi)}, \tag{9}$$

$$F_{\text{mass=const}} = \frac{1}{l} \frac{mRT \ln(V/V_{\text{i}}) - p_{\text{a}}(V - V_{\text{i}})}{\cos(\theta - \varphi) - \cos(\theta_{\text{i}} - \varphi)}. \tag{10}$$

The initial volume, V_{i}, can be found by substituting $\theta = \theta_{\text{i}}$ in equation (1). Combining equation (9) with equations (2) and (3) results in the stresses in the principal direction. In the case of principal stresses in the x-direction, the angle $\varphi = 0$. Alternatively, when there exist only stresses in the y-direction it follows that $\varphi = \pi/2$. The overall strain of the rigid-member honeycomb is related to the honeycomb angle according to

$$\varepsilon_x = \frac{\cos\theta - \sin\theta_{\text{i}}}{1 + \cos\theta_{\text{i}}}, \tag{11}$$

$$\varepsilon_y = \frac{\sin\theta - \cos\theta_{\text{i}}}{\sin\theta_{\text{i}}}. \tag{12}$$

Based on these equations, the characteristic stress–strain relations can be plotted for various values of $\rho - \rho_{\text{a}}$. This is presented in figure 6 for the case $\theta_{\text{i}} = \pi/3$, which is the default geometry for regular honeycomb. The reader might observe from these plots that there exists a highly nonlinear relationship between stress and strain in the two principal directions. Furthermore, the principal stresses vary linearly with the pressure differential.

3.1.3. Pressure-induced stiffness variation with strain. Based on the relations that have been derived in section 3.1.2, the equivalent Young's moduli in the principal $\bar{E}^{\text{p}}$ direction can be derived. Because these moduli are representative for the overall stiffness of the pressurized, rigid-member honeycomb, they are denoted by $\bar{E}^{\text{p}}_x$ and $\bar{E}^{\text{p}}_y$, respectively. They can be found by applying the chain rule in the following fashion:

$$\bar{E}^{\text{p}}_x = \frac{\mathrm{d}\sigma_x}{\mathrm{d}\varepsilon_x} = \frac{\mathrm{d}\sigma_x}{\mathrm{d}\theta} \frac{\mathrm{d}\theta}{\mathrm{d}\varepsilon_x}, \tag{13}$$

$$\bar{E}^{\text{p}}_y = \frac{\mathrm{d}\sigma_y}{\mathrm{d}\varepsilon_y} = \frac{\mathrm{d}\sigma_y}{\mathrm{d}\theta} \frac{\mathrm{d}\theta}{\mathrm{d}\varepsilon_y}. \tag{14}$$

Substituting equations (2)–(12) results in closed-form analytical expressions for $\bar{E}^{\text{p}}_x$ and $\bar{E}^{\text{p}}_y$, respectively. These expressions can easily be obtained by evaluating the partial derivatives in equations (13) and (14), but result in mathematical representations that are omitted here because they are lengthy. Full representations can be found in appendix B of [8]. A graphical representation of the (nonlinear) variation of stiffness with strain is shown in figure 7 for the case when $\theta_{\text{i}} = \pi/3$.

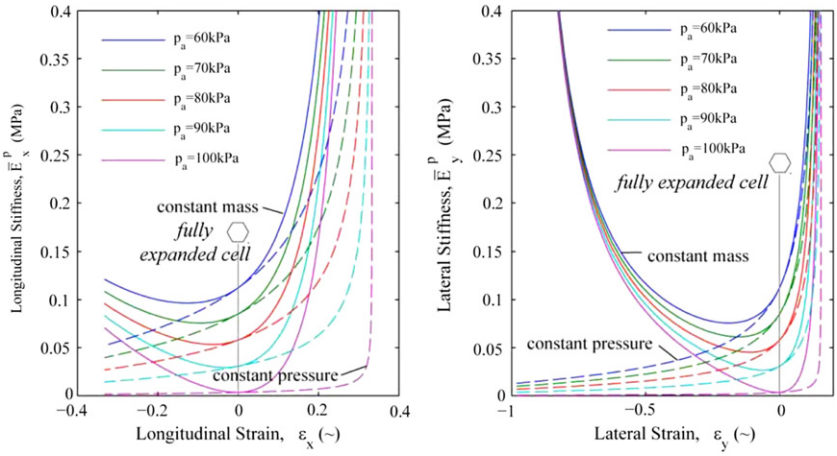

Figure 7. Stiffness variation with strain at elevated CDPs ($p = 100$ kPa).

3.1.4. Constant pressure-induced stiffness. In the present case a pressurized honeycomb is considered that forms perfect hexagonal cells when pressurized (i.e. $\theta_i = \pi/3$). In that case a constant value of the stiffness may be assumed as long as the predicted stress based on this constant value does not differ by more than 5% from the analytical value as calculated by equations (2) and (3), for the stresses in the x- and y-directions, respectively. In that case, the stiffness moduli (equations (13) and (14)) should be evaluated at $\theta = \theta_i = \pi/3$. Because of mathematical considerations (the numerator and denominator are both zero) this results in evaluating the following limits:

$$\lim_{\theta \to \theta_i = \pi/3} \bar{E}^{p}_{x} = 3\varsigma(p - p_a), \tag{15}$$

$$\lim_{\theta \to \theta_i = \pi/3} \bar{E}^{p}_{y} = 3\varsigma(p - p_a). \tag{16}$$

These simple expressions demonstrate that when the honeycomb forms perfect hexagonal cells the stiffness moduli in the x- and y-directions are identical.

By using cellular material theory (CMT, see [10]) this overall pressure-induced stiffness can be mapped onto the stiffness properties of the honeycomb ligaments. Together with the Young's modulus of the honeycomb material, E^m, a new equivalent stiffness modulus is found for the honeycomb material that accounts for both material and pressurization properties:

$$E^{eq} = E^{m} + \bar{E}^{p}_{x}\left(\frac{l}{t}\right)^{3} \frac{\sin^3\theta_i}{\cos\theta_i + 1}, \tag{17}$$

$$E^{eq} = E^{m} + \bar{E}^{p}_{y}\left(\frac{l}{t}\right)^{3} \frac{(1 + \cos\theta_i)\cos^2\theta_i}{\sin\theta_i}. \tag{18}$$

This equivalent stiffness can, in turn, be assigned to the honeycomb material, in order to analyze more complex pressure-adaptive honeycomb structures in a finite element environment. This is shown in Vos *et al* [3].

3.2. Experimental testing and correlation to the analytic model

To investigate whether the stress–strain relations of section 3.1 accurately predict the mechanics of pressurized rigid-wall honeycomb two compression tests were carried out on a multi-cell test article. This honeycomb grid was manufactured out of two-ply Kevlar laminates. All hinges were carbonized so as to minimize structural stiffness. This resulted in a structure with nearly frictionless hinges and approximately rigid walls, similar to the model presented in section 3.1. In the plane of the honeycomb cells the outer dimensions in the x- and y-directions of the honeycomb grid were 180 mm × 173 mm, respectively. The length of the specimen in the z-direction measured 290 mm. To be able to distribute a point load over the length of all the cells, c-stiffeners were bonded to the specimen such that they spanned the length of the cells. Each of the 23 cells inhibited a Mylar pouch. All the pouches were subsequently pierced by hypodermic needles, which were, in turn, connected in series by a rubber tube. By attaching the rubber tube to a pressure variation apparatus on one end and a pressure sensor on the other end the pressure in the tube could be controlled and monitored. The test specimen was positioned in an MTS858 Mini Bionix II servo hydraulic testing frame (see figure 8 for details). This machine was equipped with two caul plates between which the specimen was sandwiched.

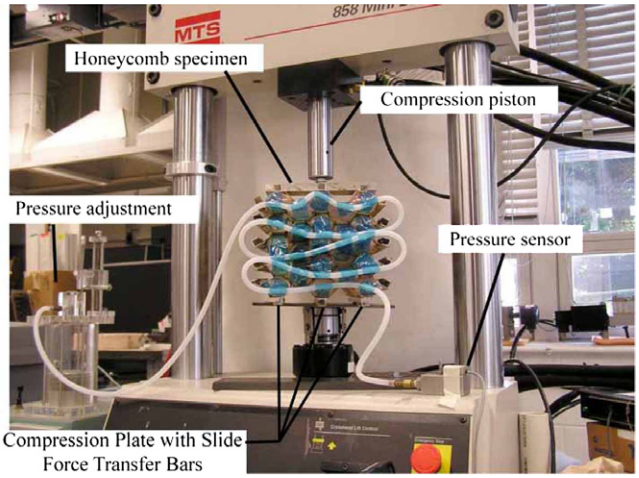

Figure 8. Experimental test setup for the rigid-wall pressure-adaptive honeycomb.

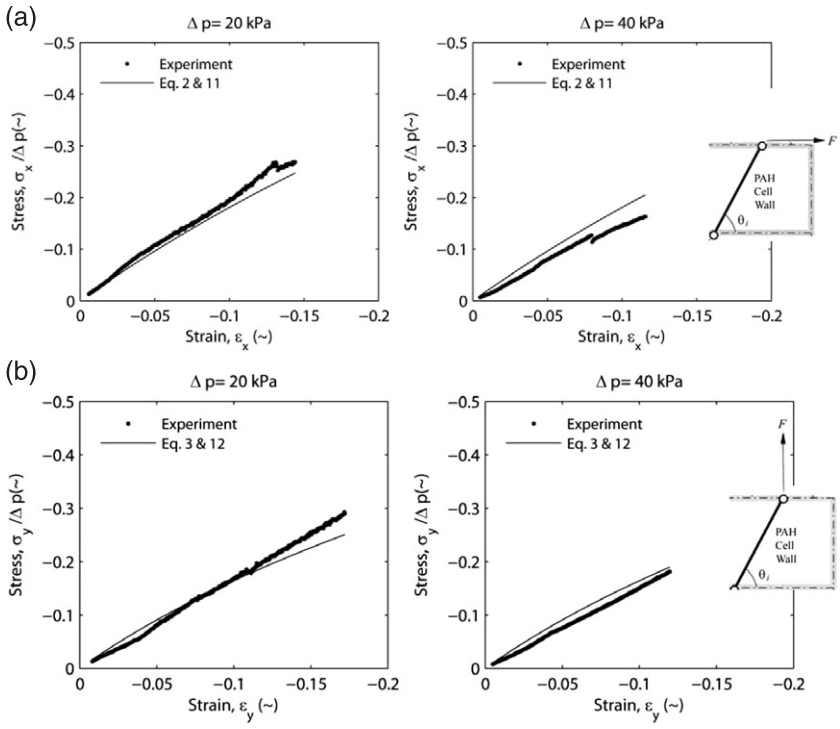

Figure 9. Stress–strain relation of the rigid-wall pressure-adaptive honeycomb. (a) Correlation between experiment and theory in the longitudinal ($\varphi = 0$ in equation (9)) direction at constant pressure. (b) Correlation between experiment and theory in the lateral ($\varphi = \pi/2$ in equation (9)) direction at constant pressure.

To allow for free lateral contraction of the specimen all the c-stiffeners were coated with a layer of Teflease. In addition the caul plates were covered with a thin layer of petroleum jelly to ensure minimum friction between the specimen and the machine. Greasing the plates ensured an almost free lateral contraction of the element during testing. Note also the continuous tube that ran from the pressurization apparatus on the left-hand side to the pressure sensor on the right-hand side. Hypodermic needles pierced through the tube on one side and into the pouches on the other side. The pressure sensor was connected to a data-acquisition unit that interfaced with Labview.

The results of the compressive test in the longitudinal direction are displayed in figure 9(a) while the results from the lateral compression tests are displayed in figure 9(b). It must be noted, however, that during this experiment the stiffness of the honeycomb structure itself contributed to the total stiffness of the system. In contrast to the single-cell experiment, this experiment, therefore, did not measure the pure pressure-induced stiffness. However, as the CDP increased, the relative stiffness of the honeycomb structure diminished and the correlation between prediction and experiment improved. However, in general, the graphs in figure 9 demonstrate a good correlation between the nonlinear analytic model and the experimental results in the longitudinal and lateral directions. This demonstrates that the model that is presented in section 3.1 appropriately captures the mechanics of the rigid-wall pressure-adaptive honeycomb.

4. Aeroelastic deformation of a pressure-adaptive flap

The goal of the wind tunnel test was to demonstrate that a pressure adaptive trailing edge could successfully alter the aerodynamic coefficients of an airfoil section. This, in turn, would prove the practical application of pressure-adaptive honeycomb as a means to provide gross deformation while under realistic aerodynamic loading. To that end, the test article was subjected to a range of velocities and angles of attack. An elaborate presentation of the resulting aerodynamic data can be found in Vos [8]. The following sections present one of the most important results, namely the aeroelastic deformation. Section 4.1 presents the test article and wind tunnel setup that was used to generate the results. In section 4.2 it is shown how a change in dynamic pressure influenced the structural deformation at various CDPs. Section 4.3 presents the effect of angle of attack on the structural deformation.

4.1. Description of the test article

The honeycomb that was used in the pressure-adaptive flap had the same cell dimensions as in previous experiments ($l = 15$ mm). Compared to the flap size ($c_f = 28$ cm), the cell was quite large. This implied that the total number of pressurized cells was limited to 13 and that the space between the upper and lower skin was not fully filled by the honeycomb. The main reason for not going to a smaller cell size lay in the manufacturing process. It was found that a honeycomb with a characteristic face length of 10 mm required

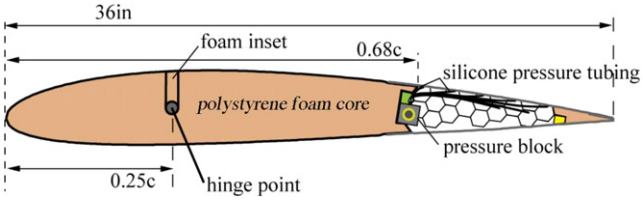

Figure 10. Sketch of the pressure adaptive honeycomb topology of the test article.

a higher level of accuracy to fabricate. Folding and bonding the honeycomb would lead to substantial misalignments that could be detrimental when pressurization was used. However, if manufacturing techniques were to improve, a smaller cell size compared to the flap dimension would be preferable. In that sense, the wind tunnel model deviated from a possible production model. A sketch of the wind tunnel model can be seen in figure 10.

The entire wind tunnel model consisted of three main parts: a main body, an adaptive flap, and a stiffened trailing edge. Both the main body and the stiffened trailing edge were made from Styrofoam by using a wire-cutting technique. The cross-sectional shape that was chosen for this wing was an NACA 2412 section (see figure 10). Two wooden templates were fabricated to use as a guide for cutting the foam to the correct shape. In a later stage, these templates were bonded to the foam to give the model a hard side surface to connect to. Small flaws in the surface of the foam model were filled in with glass putty. To give the foam model sufficient strength, it was covered in a single layer of fiber glass cloth, impregnated with epoxy. The surface roughness of the fiberglass interface was reduced by applying glass putty over its surface and sanding it down with fine-grid sand paper. A gray primer was sprayed on the surface to give the model an even smoother top layer. A thread rod with a diameter of 1.25 cm was put through the entire model at a chordwise position of $0.25c$ and on the local chord line. This provided the model with a hinge fixture for the wind tunnel. For the flap the same manufacturing techniques were used to produce the honeycomb as for the 130-cell honeycomb block. In addition, the top and bottom skins were fabricated from Al110-T3. The top skin measured 0.38 mm in thickness and was rolled (cold-worked) so as to induce an initial curvature in the flap. The bottom skin was made from 0.25 mm thick aluminum sheets. It was also rolled to an initial curvature. The honeycomb was attached to the top skin of the flap, while the bottom skin was free to translate with respect to the honeycomb. This allowed the free boundary (see figure 4) to freely contract and expand. This can be seen in the two cross-sectional views in figure 11. In these views, the flap is displayed in the retracted position where the honeycomb cells form (close to) perfect hexagons. It can also be observed how the honeycomb is clamped between the main body of the model and the foam trailing edge. The honeycomb was therefore free to expand and contract in the direction perpendicular to the top skin of the flap.

During the wind tunnel experiment various parameters were measured or controlled. The controlled parameters were

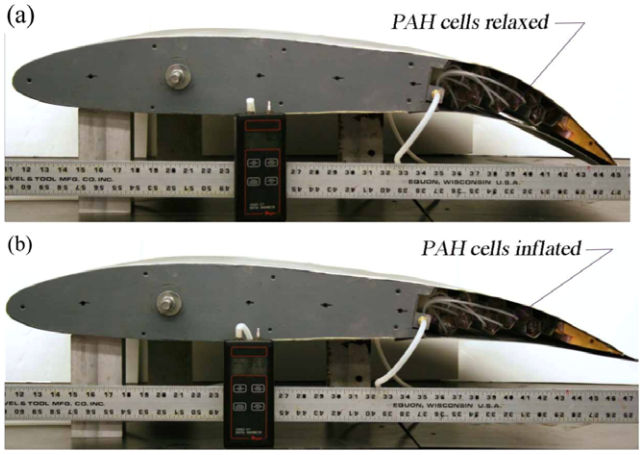

Figure 11. Test article. (a) Test article with deployed trailing edge. (b) Test article with stowed trailing edge.

the geometric angle of attack, α, the free-stream wind speed, V, and the pressure in the pouches. The measured parameters included all aerodynamic forces and moments as well as the Reynolds number, density, wind speed and cell differential pressure. The cell differential pressure was measured using a handheld manometer up to an accuracy of 0.1 kPa. The pressure difference was measured between the pressure inside the pouches and the free-stream static pressure. All the other measurements were recorded by Labview, which was connected to the wind tunnel balance sensors (forces and moments), the Pitot-static tube (velocity and static pressure) and a thermometer (static temperature). In addition, at each data point (i.e. a particular combination of the controlled parameters) a photograph was taken of the flap position.

4.2. Aeroelastic deformation due to dynamic pressure

In this section the structural deformation is presented at three different wind speeds: 15, 23, and 30 m s^{-1} (uncorrected for wind tunnel wall effects). At each of these speeds the geometry of the adaptive trailing edge was determined by means of a photograph. This was carried out at CDPs of 0 (deployed condition) and 40 kPa (stowed condition). The resulting geometry under loading was, in a post-processing step, used as an input for the panel code Xfoil. Xfoil computed the pressure distribution over the airfoil based on this input, together with the (wall-corrected) values for the Mach number, angle of attack, and Reynolds number. In figure 12 the geometric variation of the morphing trailing edge, along with its corresponding pressure distribution, as estimated by Xfoil, is shown. In addition, both the measured aerodynamic coefficients (incorporating the required wall corrections) as well as the corresponding predicted values are presented.

From a quick comparison between the graphs in figures 12(a) and (b) the conclusion can be drawn that at elevated CDP the dynamic pressure hardly has any effect on the geometry of the airfoil. On the other hand, at low or zero CDP the effect of dynamic pressure can be clearly found in the aeroelastic deformation of the aft part of the airfoil section. These findings are quantitatively supported by the aerodynamic

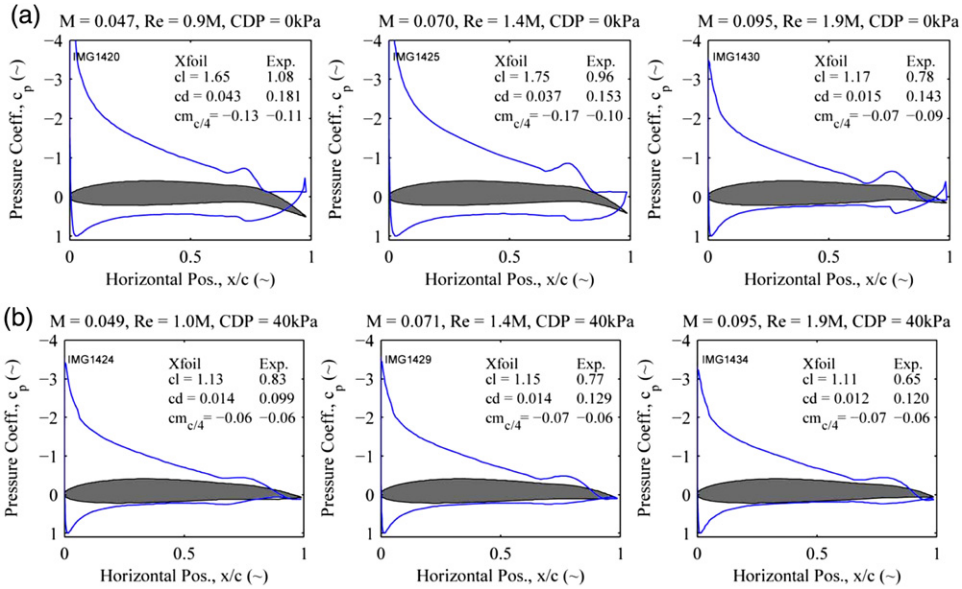

Figure 12. Effect of CDP on the aeroelastic behavior of the morphing trailing edge at various speeds. (a) Pressure distribution and aerodynamic coefficients at CDP = 0 kPa, $\alpha = 6°$, and three different speeds. (b) Pressure distribution and aerodynamic coefficients at CDP = 40 kPa, $\alpha = 6°$, and three different speeds.

coefficients, which stay fairly constant in the case of elevated CDP, but show considerable spread when the CDP = 0. Even though Xfoil predictions grossly over predict, for example, the lift coefficient, the same trends can be seen in terms of aeroelastic behavior. The relatively large discrepancy between predicted and measured results can be explained by the effects of model blockage in the wind tunnel. As was stated at the beginning of this section, manufacturing constraints of the honeycomb material dictated the size of the wind tunnel model. With a blockage percentage of more than 15%, the effect of the wind tunnel walls on the measurements could not be accurately accounted for (although this was attempted according to the methods presented in [11]).

It becomes clear from figure 12 that the effect of dynamic pressure on the geometry and hence aerodynamic characteristics of the airfoil is substantial at low or zero CDP. This is not surprising because at zero CDP the structural resistance to aerodynamic loads stems purely from the residual stiffness in the honeycomb and top and bottom skins. This allows the designer to size these components of the structure such that it displays a prescribed amount of deformation at a given airspeed. In this particular example it might be desirable to increase the residual stiffness such that somewhat less dependence of the aerodynamic properties on the dynamic pressure is encountered. There is, however, also a potential drawback that is almost classic in the design of adaptive aerostructures. Whenever a structure is stiffened to counter aerodynamic loading, it automatically means that more energy needs to be invested in order to strain this structure. In other words, a careful balance must be struck between power consumption and adverse aeroelastic deformation. Moreover, a certain amount of structural flexibility in low-speed conditions might also be beneficial for inherent gust alleviation through the adaptive nature of the structure.

4.3. Aeroelastic deformation due to angle of attack

For a wind speed of 23 m s^{-1} the effect of angle of attack on the geometry of the adaptive airfoil was investigated. Three representative angles of attack are presented: −2°, 8°, and 18°. At each of these angles of attack the geometry of the airfoil was recorded by means of photographs at CDPs of 0 and 40 kPa. Again, the resulting geometry served as an input for the panel code Xfoil, which generated a theoretical pressure distribution and aerodynamic coefficients. The results of this effort are displayed in figure 13, together with the measured aerodynamic coefficients.

The reader is asked to first consider the geometry of the airfoil at a CDP of 40 kPa (figure 13(b)). It is quite obvious that the angle of attack has hardly an effect on the geometry of the aft airfoil. The pressure-induced stiffness is simply too large to allow for any deformations under aerodynamic loading. Now, if one directs their attention to the case where the CDP = 0 (figure 13(a)), a similar behavior can be seen. The angle of attack hardly affects the geometry of the aft trailing edge. The explanation for this phenomenon can be found in the pressure distribution over the airfoil. Whereas the angle of attack change has a substantial effect on the pressure distribution over the front part of the airfoil, it shows much less change over the aft 30% of the airfoil. This confirms our observation that the adaptive structure does not change much with angle of attack, it simply does not experience a large change in load when the angle of attack is altered. In figure 13(a) a clear 'bump' in the pressure distribution can be seen over the part with the largest curvature. The resulting adverse pressure gradient on the top side of the airfoil results in a separated boundary layer according to Xfoil simulations. This separated boundary layer is absent in the pressure distributions of figure 13(b), except for the case where $\alpha = 18°$. The simulated lift curve slope for a CDP of 40 kPa is 6.4, while in the case of a CDP of zero

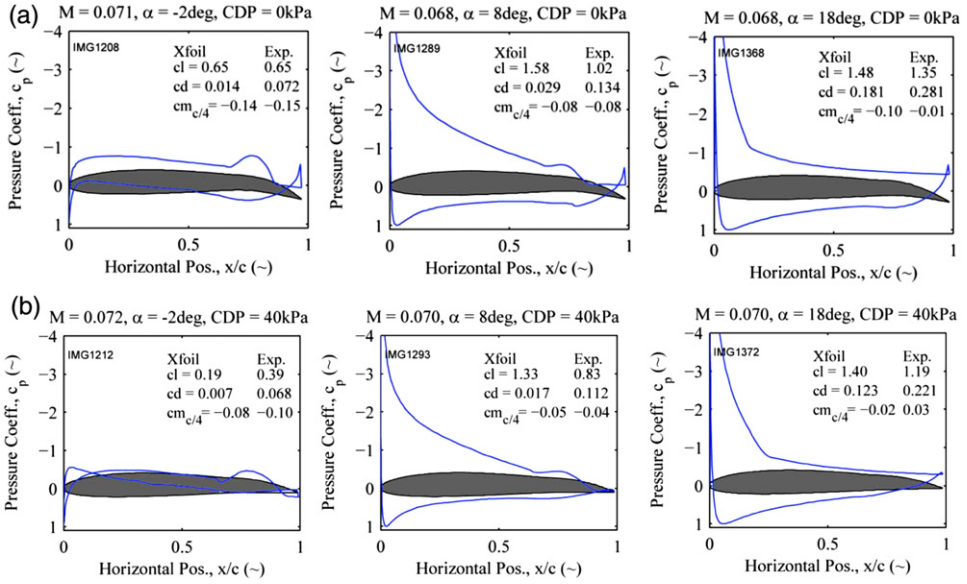

Figure 13. Effect of CDP on the aeroelastic behavior of the morphing trailing edge at various angles of attack. (a) Pressure distribution and aerodynamic coefficients at CDP = 0 kPa, $V = 23$ m s^{-1}, and three different angles of attack. (b) Pressure distribution and aerodynamic coefficients at CDP = 40 kPa, $V = 23$ m s^{-1}, and three different angles of attack.

the simulated lift curve slope is somewhat lower (5.5), which is believed to be caused by the separated flow over the aft 15% of the chord.

In practice the indifference of the aft airfoil geometry to the angle of attack is quite important. A relatively steep lift curve slope allows the pilot to make adequate changes in lift force over the wings by changing the pitch angle of the aircraft. A very shallow lift curve slope would require much larger changes of pitch angle, in order to change the lift over the wings, which is less desirable from a control point of view. The reader is cautioned that these results strictly apply to the trailing edge morphing structure. As becomes evident from the pressure distributions over the front part of the airfoil, there is a large change in aerodynamic loading when the angle of attack alters. If pressure-adaptive honeycomb were to be applied in a morphing leading edge device (such as shown in figure 3) the designer should make sure that the residual stiffness in the honeycomb structure is tailored toward the expected variation in dynamic pressure as well as angle of attack.

5. Conclusions

A new adaptive aerostructure has been presented. This pressure-adaptive honeycomb (PAH) relies on the pressurization within the cells to alter the stiffness and shape of the structure. It has been shown that the relation between the pressurization and the overall stiffness of the structure can be adequately captured by using a relatively simple analytic model. PAH has been implemented in the aft 35% of a 92 cm chord, NACA 2412 wing section and subsequently subjected to low-speed wind tunnel tests. These tests demonstrated that pressure-adaptive honeycomb could be successfully used to alter the aerodynamic characteristics of the wing section. A lift coefficient change of 0.3 was recorded for a cell differential pressure increase of 40 kPa. In addition, it was shown that the dynamic pressure of the airstream had a substantial effect on the aeroelastic behavior of the honeycomb structure, while the effect of angle of attack was essentially negligible. Future investigations will be centered on designing and constructing a pressure-adaptive honeycomb structure with tailored residual stiffness, so as to account for the aerodynamic loads that exist in various flight conditions.

Acknowledgments

The authors wish to acknowledge the generous support of the University of Kansas Transportation Research Institute (TRI) and the Aerospace Engineering Department for funding this research. The authors would also like to recognize Mr Thomas Stastny and Mr Ryan Barnhart for their tireless efforts in assisting with the fabrication of the test articles, Ms Lauren Kerth for post-processing the photographs that were taken during the wind tunnel experiments, and Mr Jan Scheepstra for assisting in preparing this article.

References

[1] Reckzeh D and Hansen H 2006 *Notes on Numerical Fluid Mechanics and Multidisciplinary Design* (Berlin: Springer) chapter (High Reynolds-Number Wind Tunnel Testing for the Design of Airbus High-Lift Wings) pp 1–8

[2] DeCamp R W and Hardy R 1984 Mission adaptive wing advanced research concepts *A Collection of Technical Papers (AIAA Atmospheric Flight Mechanics Conf.)* (Washington, DC: American Institute of Aeronautics and Astronautics)

[3] Sanders B, Crowe R and Garcia E 2004 Defense advanced research projects agency—smart materials and structures

demonstration program overview *J. Intell. Mater. Syst. Struct.* **15** 227–33

[4] Steenhuizen D, Van Tooren M J L and Vos R 2009 The application of knowledge based engineering techniques in smart concept selection for high-lift devices *20th Int. Conf. on Adaptive Structures and Technologies (Hong Kong, Oct.)*

[5] Dittrich K 2006 Cellular Actuator Device and Methods of Making and Using Same *US Patent Specificaton* 7,055782

[6] Cadogan D, Smith T, Uhelsky F and MacKusick M 2004 Morphing inflatable wing development for compact package unmanned aerial vehicles *45th AIAA/ASME/ASCE/AHS/ASC Structures, Structural Dynamics and Materials Conf. (Palm Springs, CA, April)* AIAA 2004–1807

[7] Murray G and Gandhi F 2007 Flexible matrix composite skins for one-dimensional wing morphing *48th AIAA/ASME/ASCE/AHS/ASC Structures, Structural Dynamics, and Materials Conf.* Paper 2007-1737 (Honolulu, HI: AIAA)

[8] Vos R 2009 Mechanics and applications of pressure adaptive honeycomb *PhD Thesis* The University of Kansas, Department of Aerospace Engineering Lawrence, KS

[9] Rolle K C 2005 *Thermodynamics and Heat Power* 6th edn (Upper Saddle River, NJ: Pearson Prentice Hall)

[10] Gibson L J and Ashby M F 1988 *Cellular Solids, Structure and Properties* 1st edn (Cambridge: Cambridge University Press)

[11] Barlow J B, Rae W H and Pope A 1999 *Low-Speed Wind Tunnel Testing* 3rd edn (New York: Wiley)